ELSEVIER

Contents lists available at ScienceDirect

Journal of Non-Crystalline Solids

journal homepage: www.elsevier.com/locate/jnoncrysol





Impact of strain rate on the Indentation Size Effect: Evidence of an intimate link between Size effect, Strain Rate and Ductility in Soda-lime Silica glass

Pratikshya Shrestha^a, Morten M. Smedskjaer^b, Mathieu Bauchy^c, Christian G. Hoover^{a,*}

- a School of Sustainable Engineering and the Built Environment, Ira A. Fulton Schools of Engineering, ASU, Tempe AZ 85287, United States
- b Department of Chemistry and Bioscience, Aalborg University, 9220 Aalborg, Denmark
- ^c Physics of AmoRphous and Inorganic Solids Laboratory (PARISlab), University of California Los Angeles, Los Angeles, CA 90095, USA

ARTICLE INFO

Keywords: Micro-indentation Hardness Modulus Micro-Ductility Constant strain rate Constant loading rate

ABSTRACT

Many glasses exhibit the so-called indentation size effect (ISE), where the indentation hardness decreases with the maximum applied force. Here, we seek to uncover the connection between the ISE and strain rate in sodalime silica (SLS) glass using micro-indentation. Two different loading protocols: constant loading rate (CLR), resulting in a nonlinear strain rate through the depth of indent, and a non-linear loading rate that gives a constant strain rate (CSR) with depth, are used to determine Hardness for six different strain rates and seven peak forces. A modified Bernhardt size effect law is then used to determine the extent of the ISE and load-independent hardness. We show that a small increase in micro-ductility, which can be achieved by either switching from a CLR to CSR protocol or by increasing the applied rates, can greatly reduce the extent of the ISE and slightly reduce the load-independent hardness.

1. Introduction

Transparent oxide glasses find extensive utility in diverse sectors such as windows, eyeglasses, lenses in telescopes, automotive applications, engineering materials and many more [1-4]. This societal impact has not diminished as humans physically interact with glass surfaces now more than ever—for instance, the use of glasses for panels and damage-resistant protective covers have profoundly transformed the way in which humans interact with modern touchscreen computing devices [5]. However, the increasing number of applications of glass presents numerous challenges that require careful consideration and solutions to ensure its successful integration and optimal performance. Most application design processes require the strength of a glass to be known. Indentation has been widely adopted as a well-controlled laboratory test to evaluate the strength, often measured as hardness, and other mechanical properties of glass like stiffness and ductility. Having a clear understanding of the mechanical properties of the glass is crucial when designing and selecting a glass composition for an application. One of the most challenging aspects is to understand the sensitivity of a glass's hardness not only to small variations in composition, but also testing conditions (applied force, indenter geometry, role of the environment, etc.). In particular, glass hardness often exhibits a decrease with an increase in the applied force—a behavior known as the indentation size effect (${\rm ISE}^1$).

ISE is a phenomenon which is not only seen in glasses [6–11] but also observed in ceramics [12–14], metals [15–17] and crystalline materials [18]. It is defined as the measured indentation hardness of a material being dependent on the maximum load exerted by the indenter probe on the material. More specifically, when applied forces are small, the hardness is greater than what would be measured when the applied force is larger. The ISE usually disappears for larger forces where the hardness becomes load independent [6–8]. Understanding the ISE, especially knowing at what force the load-independent hardness regime begins, is of great importance because ignoring the ISE can lead to inaccurate predictions of the glass's hardness.

The origin of the ISE in materials is a complex and highly debated topic [18–22]. Many approaches have been proposed to study and understand it including developing empirical equations [19] and using modern computational techniques like machine learning [23]. While different theories related to material behavior have also been proposed for the cause of ISE, such as subsurface cracking [22], dislocations [18], open structures [20], friction [21] and surface energy [19], further research is needed to fully understand the underlying mechanisms. Elucidating the physical nature of the ISE requires a precise

E-mail address: Christian.Hoover@asu.edu (C.G. Hoover).

^{*} Corresponding author.

¹ Indentation Size Effect

understanding of the various types of deformations that are at play upon indentation. During the process of indentation of glass, both elastic and inelastic deformation takes place [6,24,25]. All elastic deformation recovers during the unloading phase, whereas the inelastic deformation does not. The amount of irrecoverable inelastic deformation has been shown to depend on glass composition [8,26–28], maximum load applied, indenter tip sharpness, loading rates [7,24,29] and on the strain rate of the indenter probe [7].

The deformations taking place during the indentation process of silicate glass are quite complex [30]. When loads are too small for cracking to occur, it was shown that two types of irreversible deformation processes are taking place during contact loading [31]: i) shear, or plastic flow [30,32-34] that commonly results in a raised rim of glass (pile up) around the indent; and ii) densification [35-40], which can manifest as a significant increase in the refractive index, a hemispherical area of increased density, a decrease in inter-tetrahedral bonding angles and/or interatomic bonding distances, or as an increase in atomic coordination numbers. Later, it was proposed by Rouxel, Yoshida and others [25,41,42] that densification is often the controlling deformation process for glasses with low Poisson's ratio and/or low packing fraction, whereas shear flow is increasingly important for glasses with high Poisson's ratio and/or high packing fraction. It was recently revealed through using Yoshida's thermal annealing method [41] by Kazembeyki et al., that when loads are small enough to not promote cracking, the ISE in silicate glasses is controlled by the propensity for favoring either densification or shear flow [7]. In that study, the maximum force increased from 12.5 g-force (grf) up to 100 grf, and the time to reach peak loads for all tests was constant at 15 s. It was then shown that the volume fraction of glass deformed by shear flow increased with increase in peak load. It was hypothesized that this increasing shear flow volume fraction caused a reduction in viscosity of the glass near the indenter tip, resulting in the indenter probe traveling deeper than it would have if the viscosity of the glass remained high, causing lower hardness for higher peak loads. Additionally, the authors observed that load-independent region of the ISE began when the ratio of volume densified and volume deformed by shear flow, both normalized by the total inelastically deformed volume, approach constant values. The authors then showed that when comparing a deeper indent to a shallower one, at any fixed depth, the strain rate was always higher for higher peak loads, which was hypothesized to be caused by shear thinning, resulting in lower hardness values for higher peak loads. Other previous studies in the literature [43,44] have also shown that the formation of shear bands, one of the primary features that forms when glass undergoes shear flow, is strain rate dependent. Poisson's Ratio has also been shown to be a good indicator of sensitivity to strain rates [24,45], with the range of highest strain rate sensitivity found in glass with Poisson's ratio values between 0.3 and 0.4 [45]. These previous studies thus suggest that shear flow is linked to strain rate, and this prompted us to investigate this further. In this work, we introduce the term "Indentation Strain Rate Effect" (ISRE²) to describe a change in hardness when only the strain rate is changed in the loading protocol.

Strain rate (ε) is defined as change in strain per unit time $(\varepsilon = d\varepsilon/dt)$. Previously, many indentation experiments have been performed using a strain rate jump protocol to understand the strain rate sensitivity [45–47], time dependent deformation [48] and creep properties of materials [49]. However, in this study, we focus on silicate glass and do not perform the strain-rate jump test. Instead, we start by considering only protocols that involve continuous loading functions, which are typical of what most indenters can likely perform without the indenter tip suffering any damage. To accomplish this, we focus on two kinds of strain rate experiments: 1) a constant strain rate though the entire indent formation process; and 2) a traditional strain rate that decays as a power-law function, arising from applying a constant loading rate [7]

with an increasing force as the probe travels deeper into the glass. Since the subsurface strain profile can be complex [50], we rely on the indentation strain-rate (ε_i) being derived from the time-derivative of the indentation depth dh/dt. The latter is also a measure of the velocity of indenter probe divided by the displacement at time t [51], as

$$\dot{\varepsilon}_i = \frac{1}{h} \left(\frac{dh}{dt} \right) \cong \frac{\dot{h}}{h} = \frac{1}{2} \left(\frac{\dot{P}}{P} - \frac{\dot{H}}{H} \right) \tag{1}$$

where h is indentation depth, and \dot{P} are the time derivatives of the hardness and force, respectively. \dot{P} is the loading rate of a force-controlled indent. The term \dot{H}/H is usually very small and thus is typically neglected. The indentation strain rate can then be maintained constant simply by keeping \dot{P}/P constant [51]. In a typical force-controlled indentation test, \dot{P} is prescribed constant throughout the loading and unloading range; most indenters can keep \dot{P} constant. This leads to a strain rate profile that is monotonically decreasing with higher forces, arising from deeper penetration depths. For the strain rate to be kept constant throughout the loading range, a unique loading protocol is required to maintain \dot{P}/P constant. To simplify this investigation, we will focus on soda-lime silica (SLS³) glass as it is one of the most widely used glasses and has already been shown to deform predominantly through shear flow [7,52].

In summary, the work in this paper attempts to address the following questions:

- 1) How does the ISE evolve when changing the strain rate and how is this behavior different when maintaining a constant strain rate during the loading phase?
- 2) Can the term \dot{H}/H be neglected when calculating strain rates in SLS?
- 3) What differences in material behavior are occurring due to different strain rates and loading protocols?

To answer these questions, we perform micro-indentation over a wide range of strain rates and maximum forces with a Vickers probe with two different loading protocols: 1) where the loading rate is kept constant throughout the depth of an indent, which is what is commonly done in most indentation testing; and 2) where strain rate is kept constant throughout the entire indent formation process. The mechanical properties are then extracted from the load-depth response curves. We then quantify the μ -ductility of each indent and discuss the handshake between strain rate, ISE, and the μ -ductility. Note that the term ' μ -ductility' here refers to ductility on the micron scale, which is the only scale considered in this work.

2. Materials and methods

2.1. Sample preparation

In this study, we used a commercially available soda lime silica glass sample (SLS). The SLS sample had a composition of (in mol%) 73 % SiO₂, 14 % Na₂O, 9 % CaO, 4 % MgO, 0.15 % Al₂O₃, 0.03 % K₂O, 0.1 % Fe₂O₃, and 0.02 % TiO₂. The glass samples were obtained in the form of standard microscope slides measuring $75 \times 25 \times 1$ mm³, purchased from VWR Scientific Inc. Prior to experimentation, all sample surfaces were inspected and found to be smooth and free of deep scratches and cracks.

The Young's modulus of soda-lime silica is 70–72 GPa [53,54] and Poisson's ratio is 0.23 [7]. To prepare the glass samples, both sides were polished using a 1-micron abrasive disc from Buehler to achieve a smooth surface finish. The polished samples were then cleaned with isopropyl alcohol (IPA). To remove any residual internal stresses from the manufacturing process, the samples were annealed at a rate of 300

² Indentation Strain Rate Effect

³ Soda-lime Silica

K/h until they reached a temperature equal to 90 % of their glass transition temperature ($T_g=806\,$ K) in Kelvin [7,8,41,55,56]. The temperature was then maintained constant for a duration of 2 h, after which the samples were gradually cooled in a furnace. Once the annealing process was completed, the glass samples were subjected to an additional round of polishing using the same method as before. Following this, they were again cleaned with IPA. To ensure stability and to help reduce flexure of the sample during the indentation process, the annealed glass sample was rigidly attached to a metal substrate with cyanoacrylate (super) glue. This setup and preparation process was used for all experiments.

2.2. Mechanical property determination through micro-indentation

All instrumented indentation tests were conducted using the Micro Combi Tester (MCT³) from Anton Paar (formerly CSM, Neuchatel, Switzerland) [57]. The temperature in the lab during the experiments was approximately 20 °C and the relative humidity was approximately 20 %. We used a Vickers probe for all indents, which is a four-sided pyramid shape with an apical angle of 136° between opposite pyramid faces, as illustrated in Fig. 1(a). To minimize the negative influence of humidity, as shown by Fourier Transformation Infrared (FTIR) experiments [58], IPA liquid was added to the top of the sample to prevent water infiltration as seen in Fig. 1(a). When the probe makes contact with the sample, it presses into the glass creating recoverable elastic deformation (see green line in Fig. 1(b)), and permanent deformation that remains when the probe is removed from the material (Fig. 1(c)). Before any indents were performed, the tip shape function of the Vickers probe was calibrated using a fused silica standard and the software that came with the testing equipment, which followed the process described in [59]. The raw data output from each indent was a load vs. displacement curve. The influence of the compliance of the machine was subtracted out of each indentation curve before any mechanical properties were determined. Fig. 1(d) illustrates a typical curve for the SLS sample, where the maximum force applied was 50 grf.

The Vickers hardness $(H_{\rm v})$ of a material is a measure of its resistance to permanent deformation and is generally used to determine a material's mechanical strength. It is calculated by dividing the maximum force applied by the indenter probe $(P_{\rm max})$ by the surface contact area $(A_{\rm c})$ formed when the force is equal to $P_{\rm max}$, calculated by the known projected contact area shape function $A_{\rm c}=24.5~h_{\rm c}^2$, where $(h_{\rm c})$ is the contact depth [54,59],

$$H_{\rm v} = \frac{P_{\rm max}}{A_{\rm c}(h_{\rm c})} \tag{2}$$

The indentation modulus (*M*) is a measure of the elasticity of SLS and is calculated as

$$E_r = \frac{\sqrt{\pi}}{2} \frac{S}{\sqrt{A_c(h_c)}}, & M = \frac{E}{1 - \nu^2} = \frac{1}{\frac{1}{E_r} - \frac{1 - \nu_i^2}{E_i}}$$
(3)

where E_r is the reduced modulus which is obtained using properties of both the indenter tip and the material that is being indented thereby representing combined elastic response of the system. E and ν are the Young's modulus and Poisson's ratio of the material and E_i and ν_i are elastic constants for the indenter tip. Here, S represents the initial unloading slope from the load-displacement curve, as depicted in Fig. 1 (d), and A_c is the projected area calculated as previously described. The surface detection parameters used in all tests were configured with a contact stiffness that was high enough to ensure the probe contacted the glass before initiating the indentation protocol, while also preventing surface misidentification in the presence of the IPA.

In this study, we elucidate the dependence of ISE on the following strain rates: $\dot{\epsilon}=1,0.5,0.25,0.05,0.025,0.005\,\text{s}^{-1}$. This range of strain rates was chosen to keep the loading rate well within the safe operating

range of the MCT³. Two different sets of tests were conducted. In the first set, all the indents were loaded in force-control at a constant loading rate until they reached their prescribed $P_{\rm max}$. Once $P_{\rm max}$ was reached, the force was maintained constant for 10 s, and then the probe was unloaded at the same rate at which it was loaded. The loading rate was selected such that the maximum force was attained at 2, 4, 8, 40, 80, and 400 s for the strain rates investigated. These times were chosen to ensure that the average of the instantaneous strain rates during the loading segment would be approximately equal to the desired average constant strain rate from our second protocol. This first set of tests is referred to as "constant loading rate" (CLR⁴). The instantaneous strain rate during an indent at given time (t) can be determined using Eq. (1) [60], where h refers to the velocity of the probe moving through the glass and the unit of ε is in s⁻¹.

In the second set of tests, all the indents were loaded in force-control using a loading function that ensured the instantaneous strain rate was constant up until $P_{\rm max}$ was reached. This protocol is referred to as "constant strain rate" (CSR 5). At $P_{\rm max}$, the force was held constant for 10 s, and then the probe was unloaded with a linear unloading rate within 10 s. The load vs. time and strain rate vs. depth profiles for both CLR and CSR tests are shown in Fig. 2 (a-d). 3D images of the indents were obtained using Atomic Force Microscopy (AFM) and an open-source software named Gwyddion was used for surface correction to prepare the images as shown in Fig. 2(e and f). The cross-section profiles of these images at section Z-Z are shown in Fig. 2(g).

For each value of strain rate in each set of tests, an ISE study was performed. To ensure statistical significance and reliable data, a minimum of 20 indents was performed for each P_{max} (12.5, 25, 35, 50, 60, 75, and 100 grf) and at each strain rate. A diverse range of peak loads was selected, in contrast to the typical load ranges reported in the literature [41,61], while also ensuring the attainment of the load independent H_v regime. Altogether, these seven values of P_{max} and six values of $\dot{\varepsilon}$ yielded 42 different families of tests for each set (CLR and CSR). Throughout the indentation process, it was ensured that IPA remained on top of the sample to maintain consistent conditions. The overall shape of the curve was assessed for consistency before any further analysis took place, but it was typically found that most (if not all) curves from a single family overlapped with each other, indicating consistency in the indentation behavior. These curves served as the basis for subsequent calculations. The M and H_v values were determined using the continuum Oliver and Pharr model [54,59] using the software that came with the MCT³ instrument.

3. Results

3.1. Verification of Constant Loading Rates and Constant Strain Rates

We begin by first verifying that our loading protocols achieved the desired strain rates. Results are shown for both CLR and CSR testing protocols for two strain rates ($\dot{\epsilon}=0.005$ and $0.5~\rm s^{-1}$) in Fig. 3. Fig. 3(a, b, e, and f) show the mean penetration depth vs. time curves, obtained from the average of 20 indents, for each value of $P_{\rm max}$ during the loading phase. This small sampling of raw data is used to explain the method that we apply to verify the strain rates; note that this analysis was performed for every family of data. We first extract the raw h and time data for every indent performed. The raw data belonging to a single family are then averaged to get the mean h vs. time curve. We then fit a function of the form $h(t) = A \times (t)^B + C \times t$ to each of these mean curves, where A, B, and C are fitted constants, h is the penetration depth and t is time. The R-square value for all curves was greater than 0.98. The velocity curve h is then calculated from the time derivative of this function. After finding

⁴ Constant Loading Rate

⁵ Constant Strain Rate

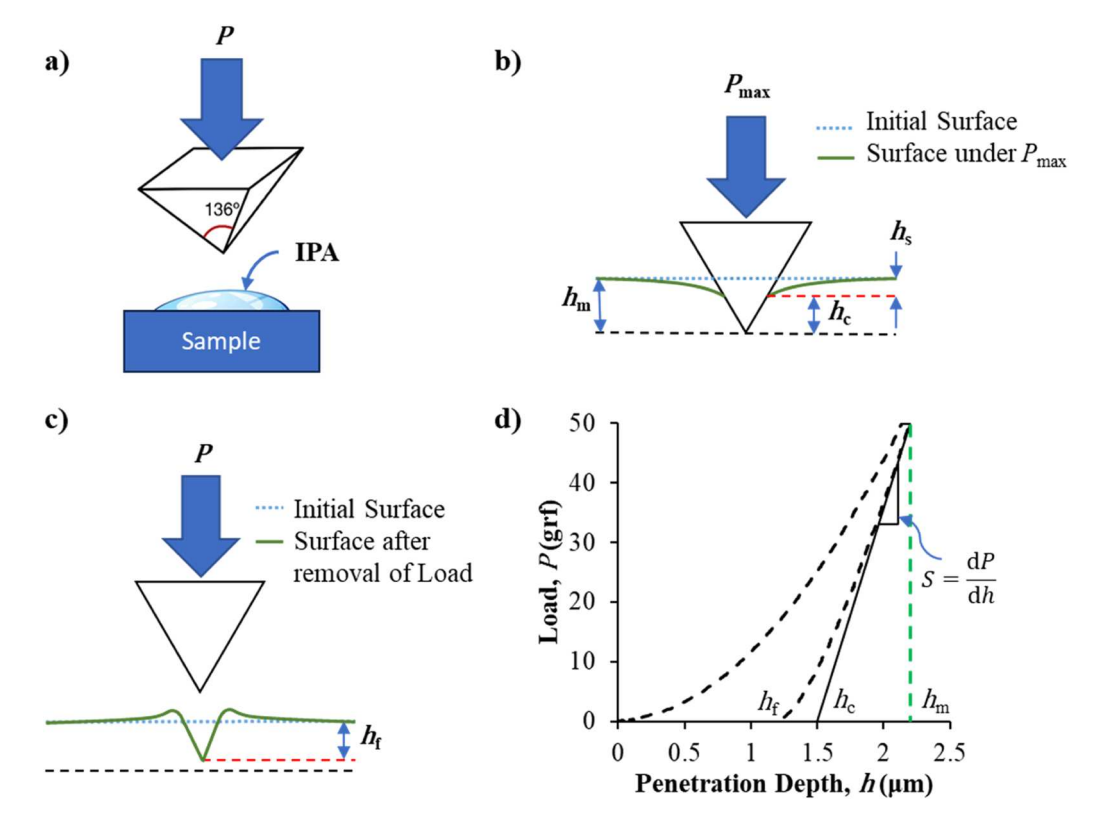


Fig. 1. (a) Schematic illustration of Vickers probe about to make contact with IPA covered glass. (b) 2D schematic illustration during maximum loading, showing contact depth (h_c), maximum penetration depth (h_m) at P_{max} and the amount of elastically recovered depth when the probe is under max force (h_s), calculated as $h_m - h_c$. (c) 2D schematic illustration of the probe and residual footprint after unloading. (d) Typical load vs. penetration depth indentation response curve for SLS at $P_{max} = 50$ grf. The contact stiffness (S), permanent depth of penetration (h_f) after the load is removed, h_m and h_c are marked.

both h and h , $\dot{\varepsilon}$ is calculated using Eq. (1) under the assumption that H is small. Here, we present $\dot{\varepsilon}$ vs. h curves from protocols designed with CLR and CSR of $\dot{\varepsilon}=0.005~{\rm s}^{-1}$ and 0.5 s⁻¹, see Fig. 3(c, d, g and h) respectfully. The CSR show an asymptotical approach of $\dot{\varepsilon}$ towards the constant value that was prescribed at high penetration depth. For the CLR curves, the $\dot{\varepsilon}$ is monotonically decreasing for increasing h. However, for each $P_{\rm max}$, taking the average of all $\dot{\varepsilon}$ and excluding values for very small h, which mathematically gives an infinite $\dot{\varepsilon}$, yield the desired average value of $\dot{\varepsilon}$ With our strain rate protocols verified, we next discuss the differences in ISE and ISRE trends to answer research question (1) from the Introduction section.

3.2. Evolution of Indentation Size Effect trends

3.2.1. Differences in ISE by CLR and CSR protocols at a fixed strain rate The mean and standard deviation of H_v obtained from both CLR and CSR protocols are listed in Tables 1 and 2, respectively. The ISE (H_v vs P_{max}) for CLR and CSR tests are shown in Fig. 4(a, b) respectively, and the ISRE (H_V vs $\dot{\varepsilon}$) data are shown in Fig. 4(c, d). The circular points represent the mean values from each family of tests and the error bars have length equal to twice the standard deviation of each family. Several overall observations can be made from these data. First, for both loading protocols in Fig. 4(a, b), a general ISE is observed for all strain rates, where H_v is larger when $P_{\rm max}$ is small, but the hardness decreases with increasing P_{max} until it eventually becomes load independent. Second, the ISE plots for both protocols show a load-independent H_v that is larger for smaller $\dot{\varepsilon}$, which results in a vertical separation of the curves for each protocol. Third, there is a general ISRE, which seems to be stronger for smaller $\dot{\varepsilon}$ (e.g., see the steep slope in Fig. 4(c)), and diminishing for larger $\dot{\varepsilon}$. Finally, the scatter for all families seems to decrease as both $\dot{\varepsilon}$ and P_{max} increase with the highest data variation being observed when $\dot{\varepsilon}$, is 0.005 s⁻¹ and P_{max} is 12.5 grf.

3.2.2. Differences in ISE caused by different $\dot{\varepsilon}$ values at a fixed protocol

Focusing specifically on the ISE trends, we observe in Fig. 4(a) that the CLR protocol shows a very strong dependence of the ISE on $\dot{\varepsilon}$, with the slower strain rates having higher hardness values for a fixed P_{max} . For faster strain rates, the ISE diminishes and H_v becomes more load independent. In Fig. 4(b), all CSR curves show a much flatter ISE, compared to the CLR protocol, and a similar decrease in H_{v} for all $\dot{\varepsilon}$ values. Both CLR and CSR protocols also show a vertical shift in the loadindependent H_v , with the smaller $\dot{\varepsilon}$ values resulting in higher H_v at a fixed P_{max} . Similar observations can be seen in the ISRE curves. In Fig. 4 (c), the CLR protocol demonstrates a very strong dependence of the ISRE on P_{\max} , with the lower P_{\max} having higher hardness values for a fixed $\dot{\varepsilon}$ However, as P_{\max} increases, the ISRE becomes less sensitive to strain rate variations, showing a flatter trend. In Fig. 4(d), all CSR curves exhibit a much less pronounced ISRE, compared to the CLR protocol, and a similar decreasing H_v strain rate effect for all P_{max} values. The primary difference between one ISRE curve and another is a vertical shift in the loadindependent H_v , where smaller P_{max} results in higher H_v values at a fixed $\dot{\varepsilon}$. Interestingly, for any value of $\dot{\varepsilon}$ except for 1 s⁻¹, H_v found by the CSR protocol is consistently lower than that found with the CLR protocol at any P_{max} , with the largest difference in value of H_v being between the lowest P_{max} of slower $\dot{\varepsilon}$ tests of both protocols. Similarly, the standard deviation, for almost any $\dot{\varepsilon}$ family, is smaller for the CSR protocol than the CLR protocol.

The percentage drop in $H_{\rm v}$ for each ISE and ISRE curve can be seen in Fig. 5(a, b). It is consistently about 5–6 % for all CSR tests, except for $\dot{\varepsilon}=0.005~{\rm s}^{-1}$ in Fig. 5(a) where it is about 9 %, and for $P_{\rm max}=100$ grf in Fig. 5(b) where it is about 3.3%. For CLR ISE tests, the percentage drop in $H_{\rm v}$ is relatively small, about 4 % for $\dot{\varepsilon}=1~{\rm s}^{-1}$ but it increases dramatically to 23 % for $\dot{\varepsilon}=0.005~{\rm s}^{-1}$. For the CLR ISRE tests, the drop in $H_{\rm v}$ increases from 7 % to 25 % as $P_{\rm max}$ decreases from 100 to 12.5 grf.

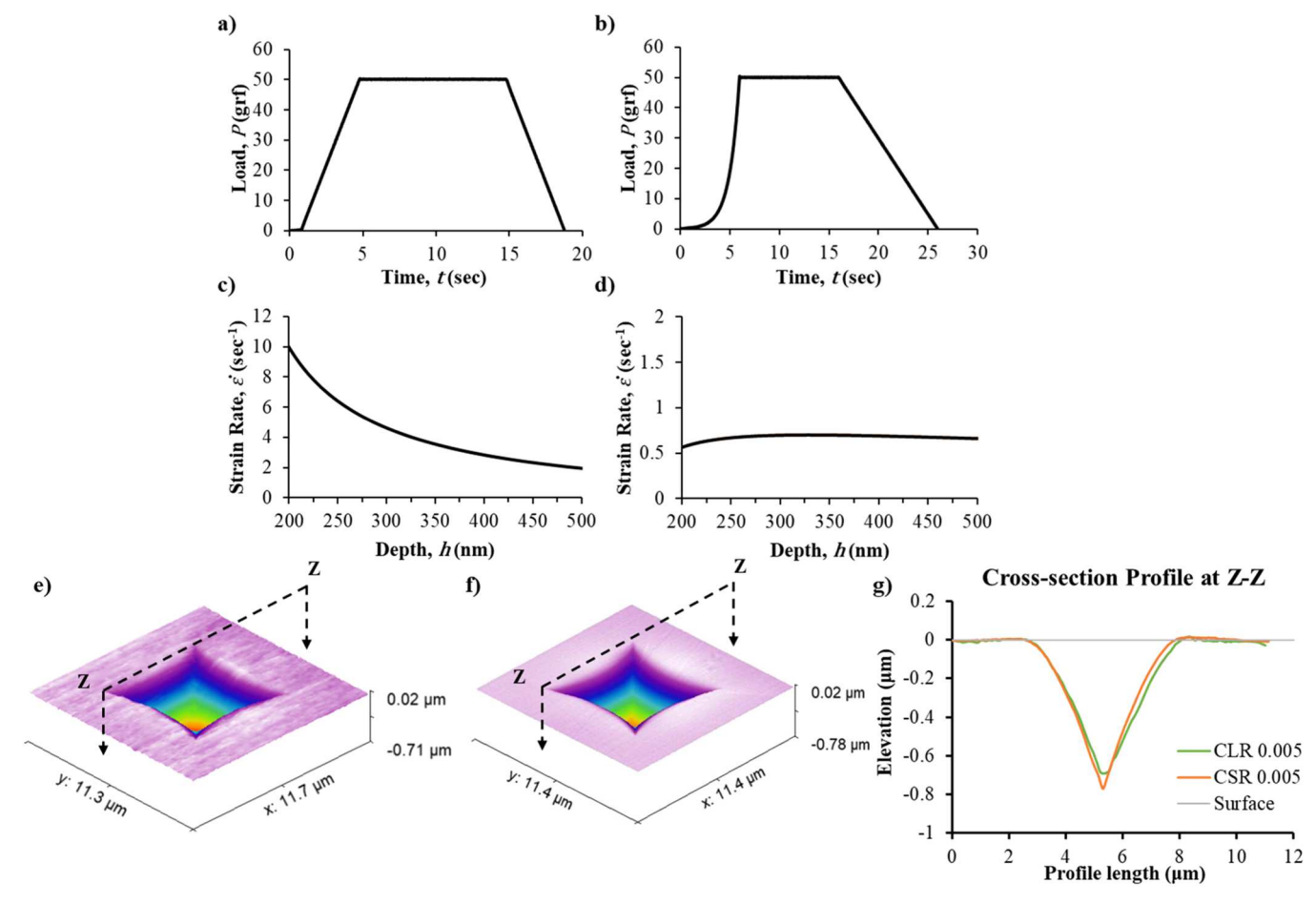


Fig. 2. (a-b) Load vs. time profile for (a) constant loading rate and (b) constant strain rate tests. (c-d) Strain rate vs. penetration depth profile for (c) constant loading rate and (d) constant strain rate tests subjected to $\dot{\varepsilon}=0.5$ and $P_{\text{max}}=50\text{grf.}$ (e-f) 3D AFM images of the indents ($\dot{\varepsilon}=0.005$ and $P_{\text{max}}=25\text{grf.}$) for (e) constant loading rate and (f) constant strain rate tests. (g) Cross-section profile at Z-Z section for (e) and (f).

4. Discussion

Several ISE studies on silicate glasses that have been carried out using micro-indentation [6-8,53]. However, some have been conducted using nano-indentation, see for example [10], due to concerns of contact area accuracies. We previously described in Section 2.2that precautions were taken, in the form of tip area function calibrations and subtraction of the frame compliance, to help minimize the inaccuracies of the technique, although we must admit that no test is perfect. Further inaccuracies can arise if large pile-up, quantified by the ratio of the final indentation depth to the depth of indentation at peak load (h_f / h_{max}) having a value of 0.7 or greater, is observed [59]. We have calculated that in these tests, all $h_{\rm f}/h_{\rm max}$ values are less than 0.56 even for the highest amount of pile-up. Therefore, the accuracy of the contact area measured by the method provided in [54,59] works well for this study. We now seek to answer research questions (2) and (3) from the Introduction section. To do this, we first consider the possibility of setting \dot{H} /H equal to zero. The discussion follows by analyzing all ISE curves and linking the trends to inelastic energy dissipation mechanisms during indentation.

4.1. Is it appropriate to set \dot{H}/H equal to zero?

Based on the data, it indeed seems appropriate to set this term equal to zero as discussed in the following. First, examining all the ISE trends for both CLR and CSR protocols in Fig. 4(a, b), we find the largest change in $H_{\rm v}$ arises from the CLR $\dot{e}=0.005\,{\rm sec}^{-1}$ protocol, between 12.5 and 25 grf. The total loading time for this protocol was 400 seconds. Since we

are looking for the largest \dot{H} , we focus on the $\dot{\varepsilon} = 0.005 \, \text{sec}^{-1}$ protocol for $P_{\text{max}} = 100 \text{grf}$, which will make the time between P = 12.5 and 25 grf the shortest for this particular $\dot{\varepsilon}$ and $P_{\rm max}$. It takes 50 seconds to reach P=12.5 grf and another 50 seconds to reach P = 25 grf. However, we do not know the H_v at this instant and in order to find \dot{H} , we can approximate the value of H_v when $P_{\text{max}} = 12.5$ grf and the time to reach it is 50 seconds by interpolating the H_v achieved from CLR 0.05(t = 40 sec) and CLR 0.025(t = 80 sec) for given P_{max} . Similarly, to find H_{v} when $P_{\text{max}} =$ 25 grf and time to reach it is 100 seconds by interpolating the H_v achieved from CLR 0.025(t = 80 sec) and CLR 0.005(t = 400 sec) for given P_{max} . We get the approximate values of $H_{12.5}$ = 762 kgf/mm² and H_{25} = 744 kgf/mm². The change in the mean H_v in this range of P_{max} is thus roughly 18 kgf/mm². This change takes place over a time of 50 seconds, making \dot{H} approximately equal 0.36 kgf/mm²/sec. Assuming this to be constant between 12.5 and 25 grf, the largest value of \dot{H}/H would then occur when H_v is minimum at 25 grf. This yields a value of \dot{H}/H of approximately 0.000484 sec⁻¹. In this same range, $\dot{P}/P = 0.01 \text{ sec}^{-1}$, which is a factor of \sim 21 higher than \dot{H}/H . This is the significantly largest change in \dot{H} . The second largest \dot{H} occurs between 25 and 35 grf for the same strain rate where $H_{25} = 744 \text{ kgf/mm}^2$ and $H_{35} = 754 \text{ kgf/mm}^2$ and this change takes place over a time of 40 s. For this range, \dot{H}/H becomes $0.000338 \text{ sec}^{-1}$ and \dot{P}/P becomes 0.00714 sec^{-1} for 35 grf, which is a factor \sim 21 higher than \dot{H}/H . Therefore, this is a sufficient difference to demonstrate that \dot{H}/H is much smaller than \dot{P}/P , meaning, \dot{H}/H is neglected in all calculations. For CSR tests, \dot{P}/P was kept constant to yield a constant ε . This agrees with the findings of Lucas and Oliver [51],

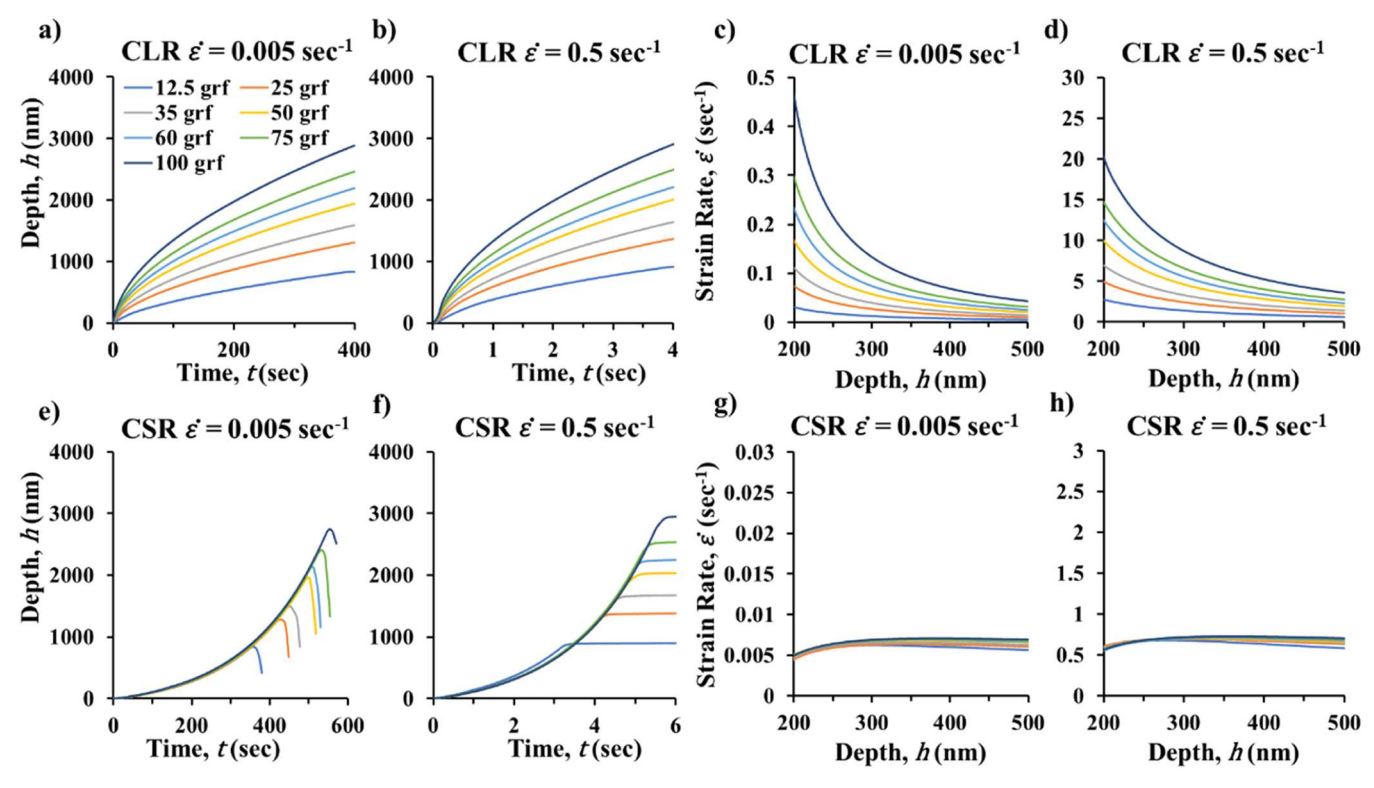


Fig. 3. (a, b, e, f) Mean penetration depth (h) vs. time (t) curves during loading phase for all P_{max} for (a, b) CLR and (e, f) CSR testing protocols for the two prescribed strain rates, $\dot{\varepsilon} = 0.005$ and 0.5 s^{-1} . Note the legend in (a) applies for all subfigures. (c, d, g, h) Resulting strain rate ($\dot{\varepsilon}$) vs. penetration depth (h) curves corresponding to h vs. t curves in subfigures (a, b, e, f).

Table 1 Mean Vickers hardness (H_V), in kgf/mm², for all 42 families of CLR tests with standard deviation.

P _{max} (grf)	$\dot{arepsilon} = 1 \ (sec^{-1})$	$\dot{arepsilon} = 0.5 \ (sec^{-1})$	$\dot{arepsilon} = 0.25 \ (sec^{-1})$	$\dot{arepsilon} = 0.05$ (sec^{-1})	$\dot{arepsilon} = 0.025 \ (sec^{-1})$	$\dot{\varepsilon} = 0.005$ (sec^{-1})
12.5	679 ±	709 ±	718 \pm	750 \pm	798 ± 88	909 ±
	41	32	25	63		148
25	667 \pm	678 \pm	692 \pm	704 \pm	742 ± 52	785 ± 67
	26	24	18	29		
35	$659 \pm$	681 \pm	$688 \pm$	707 \pm	752 ± 49	767 ± 95
	27	19	19	24		
50	666 \pm	677 \pm	682 \pm	694 \pm	712 ± 34	765 ± 43
	17	14	16	25		
60	665 \pm	675 \pm	673 \pm	692 \pm	700 ± 23	720 \pm
	13	10	16	18		107
75	663 \pm	674 \pm	677 \pm	$682\ \pm$	700 ± 29	711 ± 55
	13	11	15	16		
100	654 \pm	669 ± 8	672 \pm	$684 \pm$	686 ± 26	703 ± 48
	11		10	15		

and is further justified by the asymptotic flat line that approaches 0.005 $\rm s^{-1}$ in Fig. 3(g). Now that we have justified that \dot{H}/H can be set equal to zero, we proceed with discussing the overall trends of the ISE due to different strain rate effects.

4.2. Analysis of Indentation Size Effect

Fig. 4(a, b) show the dependence of ISE on not only protocol (CLR vs. CSR), but also the dependence on the chosen strain rate value. A generally accepted way to characterize the ISE [6] is the empirical equation proposed by Bernhardt et al. [19],

$$P = a_1 * l + a_2 * l^2 \tag{4}$$

Table 2 Mean Vickers hardness (H_V), in kgf/mm², for all 42 families of CSR tests with standard deviation.

P _{max} (grf)	$\dot{arepsilon} = 1 \ (sec^{-1})$	$\dot{\varepsilon} = 0.5$ (sec^{-1})	$\dot{arepsilon} = 0.25$ (sec^{-1})	$\dot{arepsilon} = 0.05$ (sec^{-1})	$\dot{arepsilon} = 0.025 \ (sec^{-1})$	$\dot{arepsilon} = 0.005 \ (sec^{-1})$
12.5	701 ± 34	704 ± 25	709 ± 36	711 ± 30	718 ± 36	746 ± 87
25	$\begin{array}{c} 674 \pm \\ 17 \end{array}$	$687 \pm \\15$	$\begin{array}{c} 677 \; \pm \\ 21 \end{array}$	$\begin{array}{c} 694 \pm \\ 22 \end{array}$	713 ± 41	717 ± 63
35	666 ± 13	$\begin{array}{c} 664 \pm \\ 20 \end{array}$	$\begin{array}{c} 671 \; \pm \\ 18 \end{array}$	$\begin{array}{c} 678 \pm \\ 21 \end{array}$	689 ± 38	704 ± 77
50	$\begin{array}{c} 668 \ \pm \\ 11 \end{array}$	$669 \pm \\13$	$\begin{array}{c} 671 \; \pm \\ 15 \end{array}$	$\begin{array}{c} 677 \; \pm \\ 14 \end{array}$	692 ± 25	699 ± 60
60	$\begin{array}{c} 671 \; \pm \\ 14 \end{array}$	$672 \pm \\12$	$\begin{array}{c} 676 \ \pm \\ 17 \end{array}$	$678 \pm \\15$	685 ± 15	699 ± 25
75	$\begin{array}{c} 664 \ \pm \\ 14 \end{array}$	$669 \pm \\11$	672 ± 8	$683 \pm \\13$	688 ± 18	696 ± 30
100	$\begin{array}{c} 659 \ \pm \\ 10 \end{array}$	$669 \pm \\13$	670 ± 9	$679 \pm \\11$	681 ± 13	682 ± 12

where P represents the indentation load, l is the length of the indentation diagonal in a Vickers indent footprint, a_1 represents the extent of ISE (in units of force per length), and a_2 represents the load-independent value of hardness. This equation uses the maximum force as the dependent variable and the diagonal length l as the independent variable. However, in this work, we modified this equation slightly to fit the ISE data in Fig. 4 directly. Dividing Eq. (4) by l^2 , yields

$$\frac{P}{l^2} = \frac{a_1}{l} + a_2 \tag{5}$$

where P/l^2 is proportional to the ratio of load and contact area and the equation now carries the units of hardness instead of force. Re-writing Eq. (5) using force as the independent variable yields what we refer to as the modified Bernhardt size effect law (BSEL):

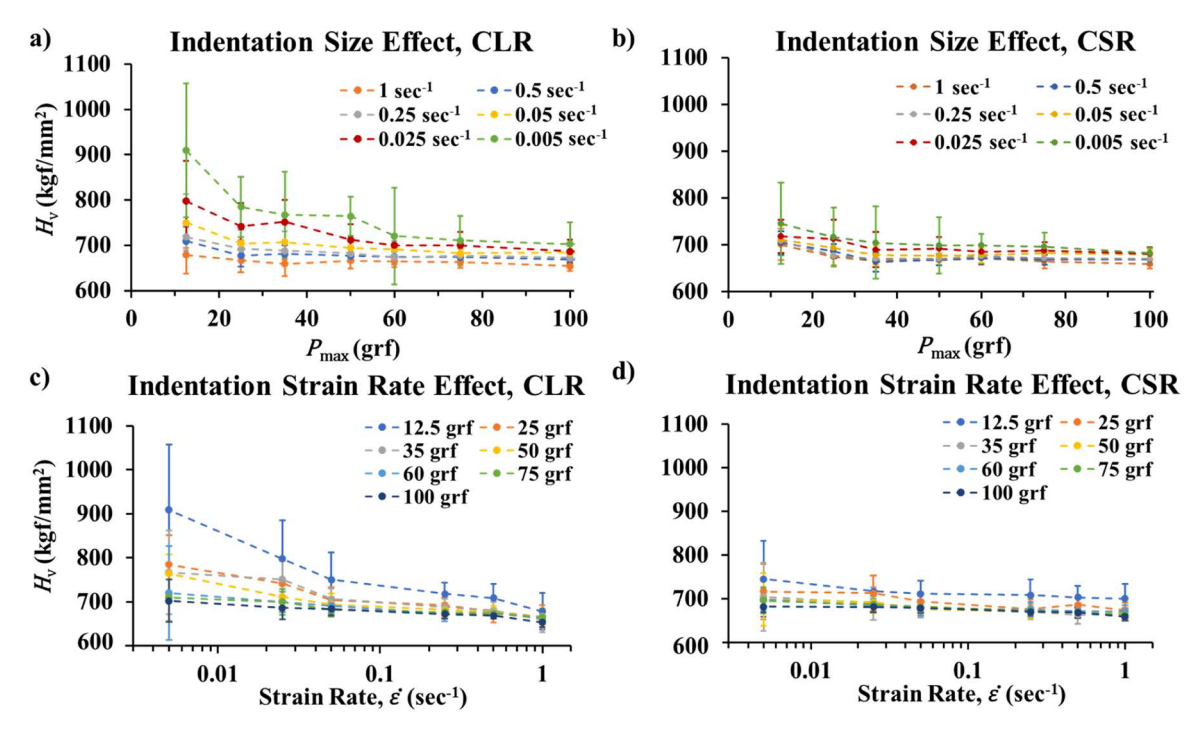


Fig. 4. (a, b) Indentation size effect on H_v for (a) CLR and (b) CSR tests. All results of the same marker color were tested with the same strain rate. (c, d) Indentation strain rate effect for (c) CLR and (d) CSR tests. All results of the same marker color were tested up to the same P_{max} . Note the strain rate axis is in logarithmic scale. For all subfigures, the markers are the mean H_v of each family of data, and the length of error bars is twice the standard deviation of that family presented in the Tables. The connecting dashed lines are to guide the eyes.

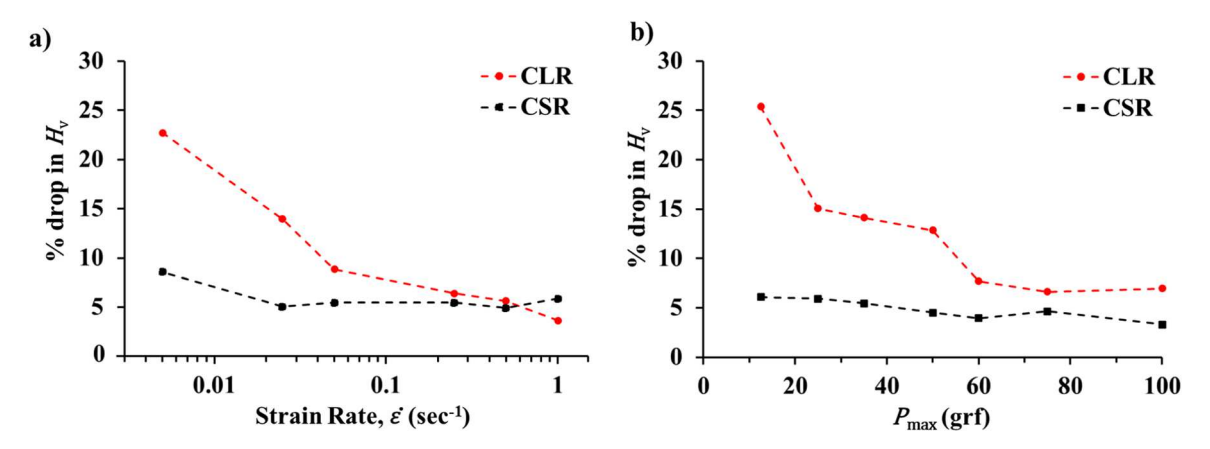


Fig. 5. Percent drop in H_v due to (a) ISE, from 12.5 to 100 grf for all $\dot{\epsilon}$, and (b) ISRE, from 0.005 to 1 s⁻¹ for all P_{max} . Results are shown for both CLR (red) and CSR (black) loading protocols.

$$H = \frac{A}{P} + C \tag{6}$$

where H is the Hardness, P is the P_{max} used to determine H, C is the load independent hardness (having the same unit as Hardness) and A is a measure of the extent of the ISE (in units of force² per length²) and controls the curvature of the ascending part of the ISE. In the following discussion, we interpret the word "extent" to mean one parameter that controls the curvature of the ISE. The greater the "extent", the smaller the radius of curvature in the ascending transition of the ISE, resulting in a larger% drop in H_v . By this definition, the CLR protocol with a $\dot{\varepsilon}$ of 0.005 s⁻¹ has the greatest "extent".

We have fit all the ISE curves from both CSR and CLR tests using Eq. (6), an example of which is shown in Fig. 6, where it is demonstrated that C is the load independent H_v . We then fit Eq. (6) to all ISE curves obtained in this study, and find the parameters A and C, which are then

graphed as the function of $\dot{\varepsilon}$ for both CLR and CSR protocols, see

Fig. 7(a-d), note that for clarity, the raw data is not shown in

Fig. 7(a, b). Note that all the curves were fitted using Trust-Region Algorithm in MATLAB with R-square value greater than 0.92 for CLR and greater than 0.81 for CSR tests. All obtained *A* and *C* values are also listed in Table 3.

The CSR ISE curves in Fig. 7(b) look very similar, with the only difference being a vertical offset between each $\dot{\epsilon}$. This is evidenced by the fact that there is only a small change in A -values, see Fig. 7(c). The slight vertical shift can be explained by the decreasing C value. Interestingly, the C values for both CLR and CSR are roughly the same for each $\dot{\epsilon}$. The biggest observed difference is the trend in A value between CLR and CSR. In log scale, the values of A from the CLR tests descend in almost a linear trend in log scale. This drastic increase in A with a decrease in $\dot{\epsilon}$ implies the extent of the CLR ISE curves are very strong for slower strain rates, which is why the curvature for slower strain rates

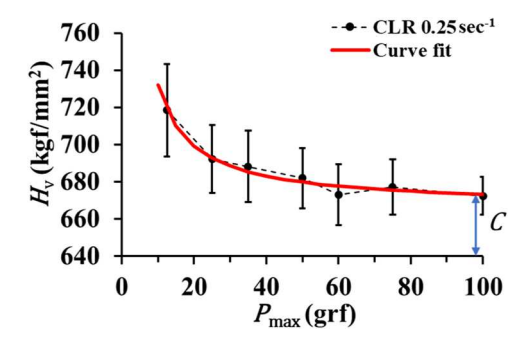


Fig. 6. Plot showing ISE in $H_{\rm v}$ using a CLR for $\dot{\varepsilon}=0.25~{\rm s}^{-1}$. The black markers are the mean $H_{\rm v}$ and the error bars have a length of twice the standard deviation for each $P_{\rm max}$. The dashed lines are to guide the eyes. The red curve is the fitted Eq. (6) for the given $\dot{\varepsilon}$. C is the load-independent hardness in the modified BSEL.

shows a sharper assent to higher H_v in Figs. 4(a) and 7(a).

4.3. What differences in material behavior are occurring due to different strain rates and loading protocols?

4.3.1. Invoking M/H as a measure of μ -ductility

Now, the ISE test results from both CLR and CSR protocols leads us to ask why these trends exist? To help answer this, we turn to a measure that implies μ -ductility, namely, the ratio of indentation modulus to Hardness (M/H) where both parameters are in the same units. In mechanical terms, M/H is equal to the inverse of yield strain and this ratio was used originally to determine different phases of heterogeneous materials [62]. It was also shown that for a purely elastic material, with no permanent deformation, M/H is equal to 2 tan $\theta=5.59$ for a Berkovich tip with a half apical angle of 70.32° [62]. Since the half apical angle for the Vickers tip used in this study is equal to 68° , the minimum value of M/H is 2 tan $\theta=4.95$. For a material experiencing ductile plastic deformation, the value of M/H increases beyond this minimum.

The increase of M/H has also been demonstrated to be positively correlated with other μ -ductility indicators like Poisson's ratio and the measure of material pile-up around the perimeter of an indent footprint [7,8,63–65]. For soda-lime silica glass, it was demonstrated in [7,8] that an increase in M/H is positively and linearly correlated with the increase in volume of shear flow (V_P), normalized with the total inelastically deformed indentation volume ($V_{\rm in} = V_{\rm D} + V_{\rm P}$) at loads small enough to not cause significant cracking, where (V_P) is a direct measure of the material deformed by shear flow and (V_D) is the volume of densified material. These studies also showed that a smaller M/H corresponds to a higher V_D/V_{in} and lower V_P/V_{in} . As M/H increased, it was observed that $V_{\rm P}/V_{\rm in}$ increased and $V_{\rm D}/V_{\rm in}$ decreased, indicating that the favored inelastic deformation mechanism transitions from a densification mechanism at low M/H, to having more influence of shear flow at higher M/H. The strong linear correlation between M/H and $V_{\rm P}/V_{\rm in}$ was also shown to exist for fully compensated calcium aluminosilicate glasses with increasing proportion of SiO₂ for a fixed peak force [8]. In this study, we simply aim to use the concept of M/H to find out if each indent favored a more densification or shear flow driven response, as this was

Table 3 Fitted parameters *A* and *C* from Eq. (6) for all ISE plots. The fitting is shown in Fig. 7.

Type of Test	Strain Rate (ε)	A -value (kgf-grf/mm ²)	C -Value (kgf/mm ²)
CLR	0.005	2857 ± 239	680.6 ± 9
	0.025	1522 ± 223	681.8 ± 8
	0.05	937.5 ± 82	674.1 ± 3
	0.25	649.4 ± 47	666.9 ± 2
	0.5	521.5 ± 68	664.7 ± 3
	1	263.6 ± 77	656.8 ± 3
CSR	0.005	817.9 ± 73	681.9 ± 3
	0.025	526.9 ± 112	679.5 ± 4
	0.05	493.8 ± 78	671.1 ± 3
	0.25	538 ± 88	661.8 ± 3
	0.5	532 ± 104	660.3 ± 4
	1	533 ± 68	656.1 ± 3

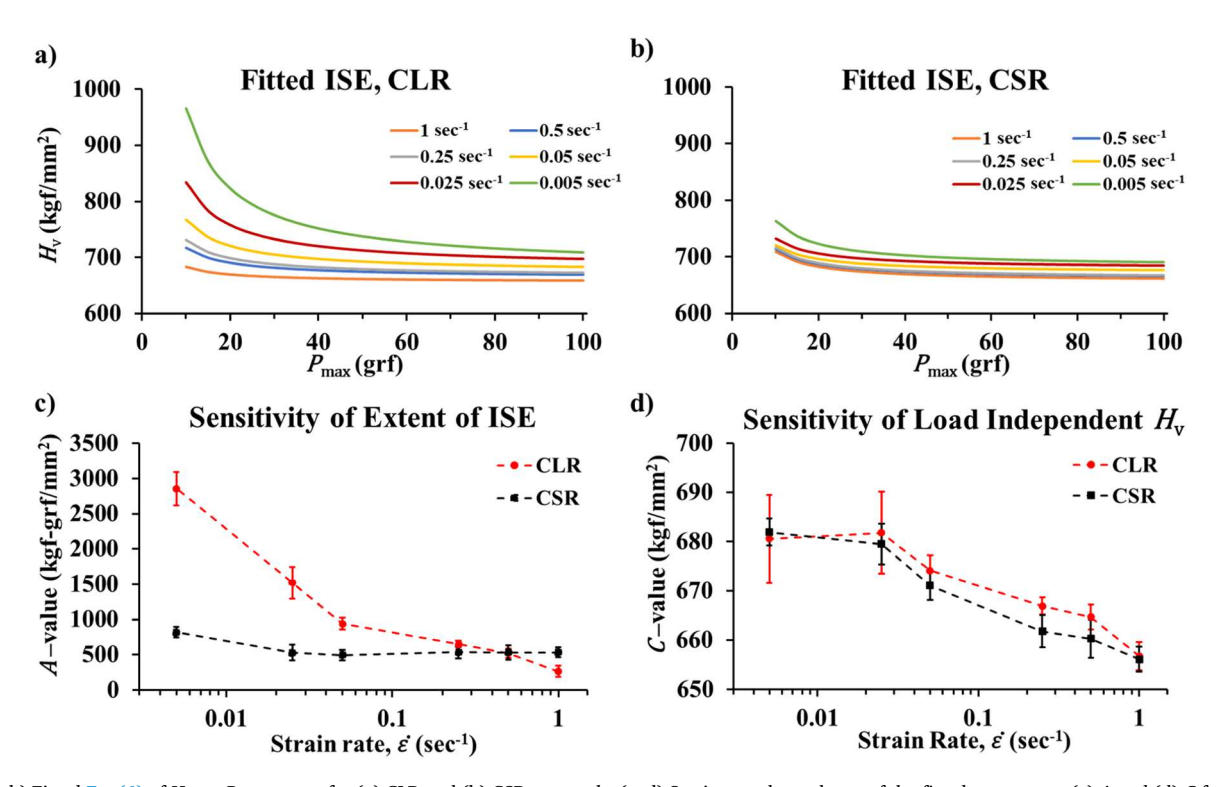


Fig. 7. (a, b) Fitted Eq. (6) of H_v vs. P_{max} curves for (a) CLR and (b) CSR protocols. (c, d) Strain rate dependence of the fitted parameters (c) A and (d) C from Eq. (6) for both CLR (red) and CSR (black) protocols. Note the strain rate axis is logarithmic.

linked to the cause of the ISE in [7].

We consider the modulus M to be a material property, that is, a quantity that, at fixed temperature, solely depends on the composition and structure of the material rather than on the testing conditions (unlike hardness). Calculating the average M for the entire collection of tests performed here yields $M=80.73\pm3.2$ GPa. All $H_{\rm v}$ values are converted to units of GPa by multiplying by the acceleration of gravity. The mean and standard deviation of M/H are then calculated for all 42 families and plotted against $P_{\rm max}$ for both CLR and CSR protocols as shown in Fig. 8(a, b). We also plot the evolution of M/H for each constant $P_{\rm max}$ as a function of strain rate for both CLR and CSR protocols as shown in Fig. 8(c, d). We notice that all M/H values are greater than 4.95 and fall within the range of 8–12, which implies that microscale plastic deformation is always taking place even for the smallest applied $P_{\rm max}$ and $\dot{\varepsilon}$. This is consistent with previous observations that glasses exhibit ductility on the micro and nano-scales [6–8,32].

4.3.2. Linking M/H trends to Indentation Size Effect behavior

Since M is a material constant that is independent of the strain rate and maximum load, M/H in this study on SLS glass solely depends on the value of H_v . If H_v is small, M/H will be large, indicating that the indent will favor a more ductile response than one with a higher H_v . First, focusing on the ISE plots for both protocols in Fig. 8(a, b), we find that M/H increases with an increase in $P_{\rm max}$ up to a certain point and then seems to asymptotically approach a constant value. Interestingly, the load independent force range of M/H for each strain rate is same as the load independent range for H_v for a given strain rate, indicating a strong link between the ISE and evolution of μ -ductility. The transition to a more ductile behavior at a higher peak force was first shown in [7] to also be linked to the cause of the ISE, i.e., the more ductile the response, the lower H_v . For example, the largest increase in M/H observed for the CLR protocols is found between 12.5 - 60 grf for $\dot{\varepsilon} = 0.005 \, {\rm s}^{-1}$ (Fig. 8(a)). This is the same force range where a steep decrease is noticed for H_v in

Fig. 4(a). Such a large increase of M/H in this force range suggests a large increase in $V_{\rm P}/V_{\rm in}$ and a transition to a much more ductile behavior at higher loads. Beyond 60 grf, both M/H and $H_{\rm v}$ remain approximately load independent, indicating no further increase in μ -ductility. A previous study [43] demonstrated that with longer time available at lower loading rates, a higher concentration of shear bands was observed near the top periphery of indents and vice versa for higher loading rates. This higher number of shear bands might be attributed to some portion of inelastic energy being used in creating a greater number of shear bands at lower loading rates. This could explain why M/H or the μ -ductility of the glass is lower for slower strain rates. Invoking the conclusions from [7], the load independent range is also when the proportions of $V_{\rm P}/V_{\rm in}$ and $V_{\rm D}/V_{\rm in}$ are constant.

In contrast, the load dependence of M/H dissipates for higher strain rates, which is accompanied by a reduction in the load dependence of H_{v} (Fig. 5(a)), indicating a minimal increase in μ -ductility. Additionally, it is observed that higher $\dot{\varepsilon}$ values, for both protocols, also have larger M/Hvalues for each P_{\max} when compared to protocols with lower $\dot{\varepsilon}$ values, as demonstrated in Fig. 8(c, d). This suggests that at a fixed P_{max} , a higher $\dot{\varepsilon}$ induces a more ductile response than a lower $\dot{\varepsilon}$. Finally, the error bars for slower $\dot{\varepsilon}$ are longer than for faster $\dot{\varepsilon}$, which suggests that the randomness of the indentation results on SLS could also be strain rate dependent. At faster $\dot{\varepsilon}$, M/H is higher which implies that μ -ductility of material is higher, and indent is subjected to larger plastic zone under the indenter tip. The enhanced μ -ductility at these faster $\dot{\varepsilon}$ allows the material to yield more readily, effectively smoothing out any surface imperfections or irregularities during the indentation process. This smoothing effect, caused by the material's increased plastic flow under higher strain rates, is likely the reason why the faster $\dot{\varepsilon}$ tests exhibit shorter error bars and reduced data scatter in the measured H_v . Conversely, at the slowest $\dot{\varepsilon}$, the material's ductility is relatively lower, and the smaller plastic zone generated during indentation is less effective in mitigating the influence of surface imperfections or material variability, leading to longer error

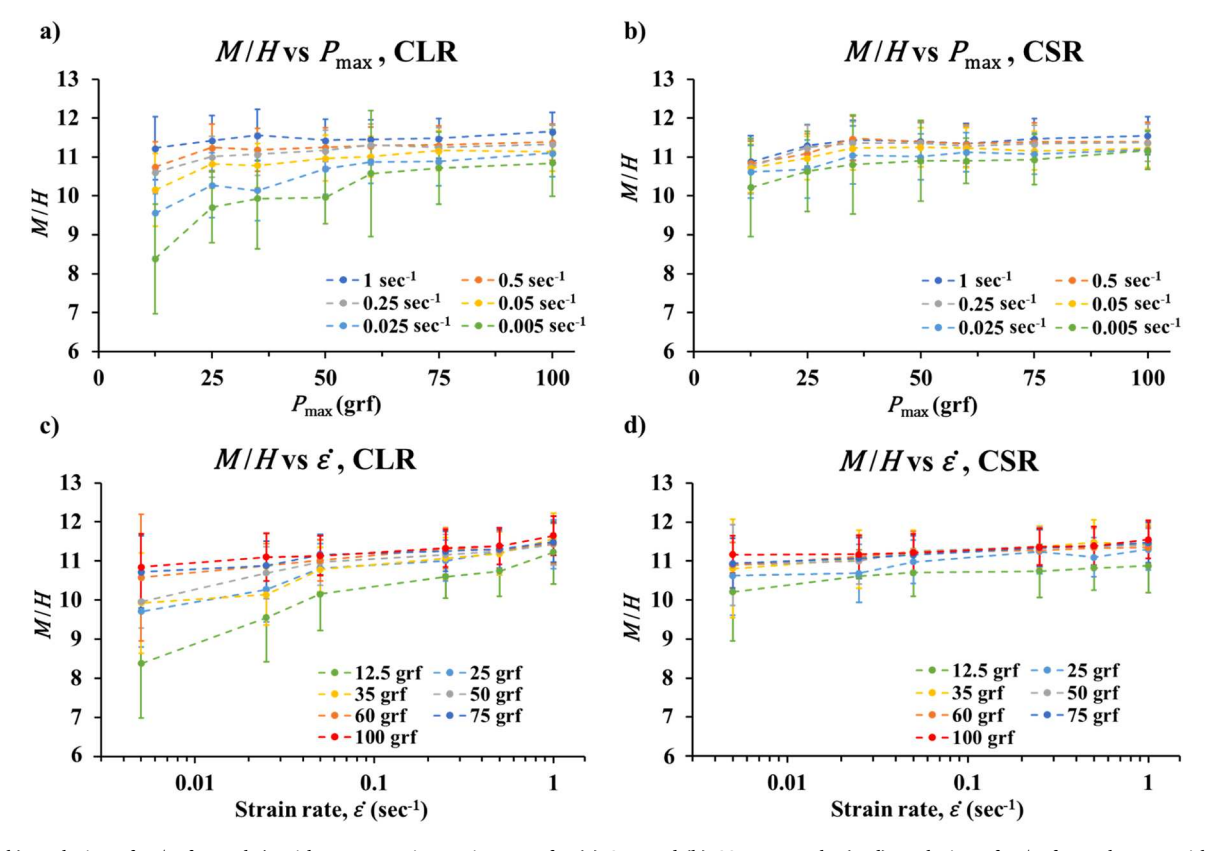


Fig. 8. (a, b) Evolution of M/H for each $\dot{\epsilon}$, with respect to increasing P_{max} for (a) CLR and (b) CSR protocols. (c, d) Evolution of M/H for each P_{max} , with respect to increasing $\dot{\epsilon}$, for (c) CLR and (d) CSR protocols. All values of M/H are above 4.95 even for small values of P_{max} , indicating presence of μ -ductility.

bars and larger variability in the results. Similarly, at lower $P_{\rm max}$, the indenter penetrates to shallower depths into the material surface. This shallow indentation depth makes the measurement of $H_{\rm v}$ highly sensitive to any potential surface imperfections or small variations in material properties arising from factors such as non-uniform surface polishing or pre-existing deformities resulting in longer error bars for lower $P_{\rm max}$.

Combining these observations, it becomes evident that for the CLR protocol, the ISE is strongly dependent on the strain rate. That is, the smaller the strain rate, the larger the change in favored inelastic energy dissipation, accompanied by a large drop in $H_{\rm v}$. The largest ISE is observed for the slowest $\dot{\varepsilon}$ of $0.005~{\rm s}^{-1}$. The largest $\dot{\varepsilon}$ of $1~{\rm s}^{-1}$ is high enough to cause the indentation response for all forces in the investigated range to be dominated more from μ -ductility, thus effectively reducing the effect of ISE. All strain rates between these two values experience a transition from a strong change in favored inelastic energy dissipation mechanism, causing a strong ISE, to almost no change in favored inelastic energy dissipation mechanism resulting in weak or no ISE.

Focusing next on the CSR ISE data in Fig. 8(b), we note four primary observations. First, like the CLR protocol, at each P_{max} the faster the applied $\dot{\varepsilon}$, the larger the value of M/H, supporting the conclusion that higher $\dot{\varepsilon}$ induces a more ductile response than a lower $\dot{\varepsilon}$. Second, the range of values of M/H for the CLR protocol was observed to be \sim 8–12, whereas for the CSR protocol, this range is narrower, usually ranging from 10 to 11, with values consistently exceeding the minimum value of 4.95. Third, all load dependent M/H values for a fixed $\dot{\varepsilon}$ are lower for the CLR protocol than for the CSR protocol. This suggests that the CSR protocol induces a more ductile response when compared to the CLR protocol at a fixed $\dot{\varepsilon}$. Finally, and perhaps the most noticeable difference between the CLR and CSR test results, the change in M /H through the force range at a fixed strain rate is essentially the same for all $\dot{\varepsilon}$. In other words, each CSR used in this study appears to have the same small transition to a slightly more ductile response throughout the same force range, resulting in roughly the same small change in H_v for all CSR ISE results (see the almost equal% drop in H_v for all CSR protocols in Fig. 5

4.4. Evolution of A and C parameters in modified Bernhardt Size Effect Law

Finally, we attempt to link the parameters of the modified BSEL to the changes in μ -ductility and observations from the ISE and ISRE. We first consider the load independent regions in the ISE data in Fig. 4(a, b) and in the μ -ductility evolution in Fig. 8(a, b). In this load-independent range, at a fixed $P_{\rm max}$, the μ -ductility M/H increases with increasing strain rate, whereas C, the load independent hardness, decreases for both CLR and CSR protocols. This shows an inverse relationship between μ -ductility and C for all strain rates.

Considering Fig. 7(c), a higher A value corresponds to a larger transition (change in M/H) from brittle to ductile for a given strain rate. For strain rates that show almost no change in μ -ductility, including all tests in the CSR protocol, A is very small. However, for strain rates that show a large change in μ -ductility, A is significantly larger.

4.4.1. Linking load independent Hardness to material behavior

First, we discuss the trend for the load-independent hardness parameter C. Consider a fixed $P_{\rm max}$, in both protocols, M /H increases with an increase in strain rate, as observed in Fig. 8(c, d). Invoking the idea of the shear thinning thought model summarized for SLS and glassy silica from [7], we consider the link between stress, strain rate, and viscosity. For lower strain rates, the stress will increase proportionally with the applied strain rate, an indication of a Newtonian response. The viscosity, which is the stress divided by the strain rate, will thus remain constant for small strain rates. Shear thinning is a phenomenon where the viscosity of the glass decreases with increasing strain rates. This is

caused by the stress, or in the case of indentation H_v , asymptotically approaching a constant value for increasing strain rates. More information on shear thinning can also be found in [66,67]. We then consider the instantaneous strain rates reached for the CLR protocol for 0.005 and 0.5 s $^{-1}$ in Fig. 3(e, f). At any fixed depth, the instantaneous strain rate for the 0.5 s $^{-1}$ rate is higher than that for the 0.005 s $^{-1}$ rate. As an example, at 200 nm, the instantaneous strain rate for the applied 0.005 s $^{-1}$ rate is approximately 0.45 s $^{-1}$, whereas for the 0.5 s $^{-1}$ rate, it is approximately 20 s $^{-1}$. The same observation is made for the CSR protocol, where the instantaneous strain rate is equal to the applied strain rate. Coupling this observation with the fact that μ -ductility increases with strain rate gives the hypothesis that the viscosity of a certain zone or volume of the glass under the indenter tip must decrease for increasing applied strain rates, independent of the protocol.

To further justify this, we note that the probe reaches the peak force within a few seconds at the higher strain rates used in this study. This likely results in an increase in temperature due to atomic structural rearrangement of the material being sheared, which is likely because SLS contains about 14 % Na₂O and 9 % CaO that act as network modifiers. The addition of these modifiers is generally done to increase the formability and to lower the $T_{\rm g}$ value of glasses. However, this also reduces the connectivity of the structure and promotes shear flow. The larger the strain rate, the larger the reduction in viscosity and the larger the zone of plastic material under the indenter tip. The lower viscosity allows the probe to penetrate more easily through the material, resulting in deeper penetration depths and, consequently, a lower load-independent hardness (C-value) for larger applied strain rates. This link demonstrates the strong connection between C, M/H and $\dot{\varepsilon}$, independent of the protocol.

4.4.2. Linking A -value to μ -ductility and strain rate

Next, we consider the link between the parameter A, M/H and $\dot{\varepsilon}$. From Fig. 7(c), it is evident that A decreases rapidly for the CLR protocol with increasing $\dot{\varepsilon}$, signifying a strong reduction in the extent of ISE for larger strain rates. Notably, at higher values of A, corresponding to slower strain rates, there is a larger transition in material behavior from being less influenced by μ -ductility at a lower P_{max} , to being more influenced by μ -ductility at a higher P_{max} , demonstrated by the larger change in M/H through the same range of P_{max} (Fig. 8(c, d)). Conversely, we observe that faster strain rates are accompanied by lower A-values, indicating a smaller change in the influence of μ -ductility. Therefore, A can additionally be considered as a parameter that not only implies the curvature of the ISE trend and% drop in ISE, but also as a parameter that implies the transition of material behavior from less influenced by μ -ductility to more influenced. Specifically, the larger the A -value, the larger the transition in the material's influence in μ -ductility and smaller is the radius of curvature in the ISE trend. These conclusions also hold true for the CSR protocol. We note that there is minimal change in A for the CSR protocol as a function of $\dot{\varepsilon}$ (Fig. 7(c)). If this hypothesis is correct, it should be accompanied by a minimal variation in M/H for a fixed strain rate and this is what is seen in Fig. 8(d). Therefore, for any strain rate in the CSR protocol, there is almost no transition in material's influence from μ -ductility, irrespective of the magnitude of applied peak forces applied in this study. We recognize that this hypothesis is purely based on the observations in this study and should be further tested on glasses with different compositions and deformation mechanisms.

4.4.3. Relation between μ -ductility and strain rate for CLR and CSR protocols

To further investigate the link between μ -ductility and strain rate, we plot the A and C values from the modified BSEL vs. strain rate and M/H, at $P_{\rm max}$ of 100 grf, for both protocols (Fig. 9). Note that these plots are like those in

Fig. 7(c, d), with the inclusion of the μ -ductility evolution. It appears that all curves in each plot (panels a through d) very closely overlap, further suggesting that the extent of the ISE and load-independent

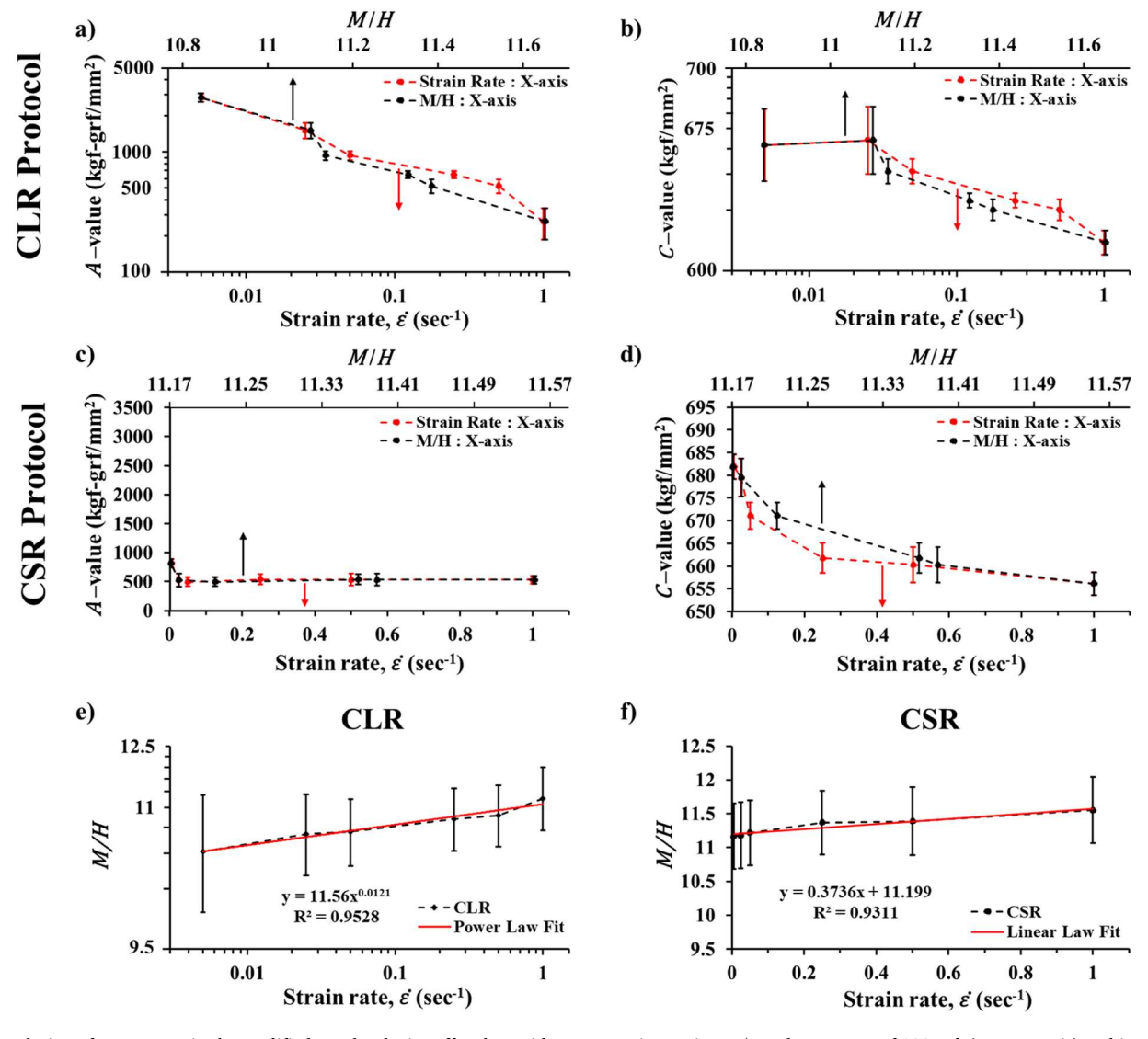


Fig. 9. Evolution of parameters in the modified Bernhardt size effect law with respect to increasing M/H, taken at P_{max} of 100 grf, (upper X-axis) and increasing $\dot{\epsilon}$ (lower X-axis). (a) A and (b) C parameters for CLR protocol, and (c) A and (d) C parameters for CSR protocol. Note the $\dot{\epsilon}$ axis and y-axis scale is logarithmic for panels (a) and (b) and linear for panels (c) and (d). Also note, for clarity, only the standard deviations for the A and C values are shown for all plots. (e, f) Load independent M/H vs $\dot{\epsilon}$ of P_{max} =100 grf along with fitted curves (red) for (e) CLR protocol (f) CSR protocol. Note that both X and Y axes are in logarithmic scale for panel (e).

hardness evolve as a function of M/H and $\dot{\varepsilon}$ in the same way for each protocol. This further supports the strong link and dependence of strain rate on μ -ductility. It is interesting to note the overlap for the CSR protocol is achieved quite well with all the axis in linear scale. However, the overlap is not possible for the CLR protocol unless the strain rate and yaxis are both in logarithmic scale. This motivated us to remove the axis in common, the parameter axis, and plot how M/H evolves vs $\dot{\varepsilon}$ for each protocol, see Fig. 9(e and f). Here, we see the trend of M/H vs $\dot{\varepsilon}$ for both protocols. Please note that both the x and y axis for the CLR protocol are in log scale and are in linear scale for the CSR protocol. This mandates that the mathematical link between μ -ductility and strain rate is a power law for the CLR protocol, with an exponent equal to the slope of the linear trend in the log vs log scale, and a linear equation for the CSR protocol. We believe the reason for these trends might be due to the instantaneous strain rate trends through the depth of the indent, see Fig. 3. The CSR protocol maintains mostly a constant instantaneous strain rate through the indent depth. However, the CLR protocol caused the instantaneous strain rate to have a decaying power law trend through the depth.

5. Conclusion

Overall, our findings underscore the intimate relationship between strain rate ($\dot{\epsilon}$) and the extent of the indentation size effect (ISE) as well as the influence of μ -ductility on the indentation behavior of soda-lime silica glass. We demonstrated that the ISE, while more pronounced at slower $\dot{\epsilon}$, exhibited a diminishing influence with increase in $\dot{\epsilon}$ for constant loading rate (CLR) tests whereas little influence from $\dot{\epsilon}$ was observed for the constant strain rate (CSR) tests. This outcome also validates the material's sensitivity to different strain rate protocols, with slower $\dot{\epsilon}$ emphasizing large change in the influence of μ -ductility and higher $\dot{\epsilon}$ leading to more consistent hardness values with more constant influences of μ -ductility for the CLR protocol. However, for CSR protocol, almost no transition in material behavior was observed, emphasizing a more constant influence of μ -ductility throughout the range of forces and strain rates used in this study.

We have also shown that the time derivative of Hardness (\dot{H}) is very small and plays almost no role in calculating the indentation strain rate which is justified by the significant difference between the values of \dot{H}/H and \dot{P}/P . The analysis of ISE curves by fitting the modified Bernhardt

Size Effect Law parameters, helped us to further describe the material behavioral differences attributed to various strain rates and different loading protocols. We showed that increase in μ -ductility, whether by increasing the magnitude of peak force or strain rate, is responsible for mitigation of the extent of the ISE at the expense of a slight reduction in load independent Hardness. We have also demonstrated that the amount of μ -ductility can be increased by indenting at a constant strain rate rather than constant loading rate. This demonstrates that the intimate link between strain rates, loading protocols and material behavior can be understood from the analysis of the ISE. Overall, this study offers a comprehensive understanding of the intricate connections between ISE, strain rates, and material responses during indentation.

CRediT authorship contribution statement

Pratikshya Shrestha: Writing – review & editing, Writing – original draft, Validation, Supervision, Methodology, Investigation, Formal analysis, Data curation. Morten M. Smedskjaer: Writing – review & editing, Methodology, Conceptualization. Mathieu Bauchy: Writing – review & editing, Resources, Methodology, Conceptualization. Christian G. Hoover: Writing – review & editing, Writing – original draft, Supervision, Methodology, Investigation, Funding acquisition, Conceptualization.

Declaration of competing interest

The authors declare that they have no known competing financial interests or personal relationships that could have appeared to influence the work reported in this paper.

Data availability

Data will be made available on request.

Acknowledgments

This work was supported by the National Science Foundation under Grants No. 2145807 and 1826050. M.B. acknowledges support from the National Science Foundation under Grant DMR- 1944510 and M.M.S. acknowledges support from the European Union (ERC, NewGLASS, 101044664). Views and opinions expressed are, however, those of the authors only and do not necessarily reflect those of the European Union or the European Research Council. Neither the European Union nor the granting authority can be held responsible for them. The authors would also like to thank Seetha Pavan Tanneru for all his hard work in helping with laboratory testing. During the preparation of this work the author (s) used ChatGPT in order to improve language and readability. After using this tool/service, the author(s) reviewed and edited the content as needed and take(s) full responsibility for the content of the publication.

References

- [1] A. Ellison, I.A. Cornejo, Glass substrates for liquid crystal displays, Int. J. Appl. Glass Sci. 1 (2010) 87–103, https://doi.org/10.1111/j.2041-1294.2010.00009.
- [2] E. Axinte, Glasses as engineering materials: a review, Mater. Des. 32 (2011) 1717–1732, https://doi.org/10.1016/j.matdes.2010.11.057.
- [3] T. Maeder*, Review of Bi2O3 based glasses for electronics and related applications, Int. Mater. Rev. 58 (2013) 3–40, https://doi.org/10.1179/ 1743280412Y.0000000010.
- [4] J.C. Mauro, E.D. Zanotto, Two centuries of glass research: historical trends, current status, and grand challenges for the future, Int. J. Appl. Glass Sci. 5 (2014) 313–327, https://doi.org/10.1111/ijag.12087.
- [5] J.C. Mauro, Grand challenges in glass science, Front. Mater. (2014) 1. htt ps://www.frontiersin.org/articles/10.3389/fmats.2014.00020. accessed July 10, 2023.
- [6] M.M. Smedskjaer, Indentation size effect and the plastic compressibility of glass, Appl. Phys. Lett. 104 (2014) 251906, https://doi.org/10.1063/1.4885337.

- [7] M. Kazembeyki, M. Bauchy, C.G. Hoover, New insights into the indentation size effect in silicate glasses, J. Non-Cryst. Solids 521 (2019) 119494, https://doi.org/ 10.1016/j.inoncrysol.2019.119494.
- [8] M. Kazembeyki, K. Yang, J.C. Mauro, M.M. Smedskjaer, M. Bauchy, C.G. Hoover, Decoupling of indentation modulus and hardness in silicate glasses: evidence of a shear- to densification-dominated transition, J. Non-Cryst. Solids 553 (2021) 120518, https://doi.org/10.1016/j.jnoncrysol.2020.120518.
- [9] G.D. Quinn, P. Green, K. Xu, Cracking and the indentation size effect for knoop hardness of glasses, J. Am. Ceram. Soc. 86 (2003) 441–448, https://doi.org/ 10.1111/i.1151-2916.2003.tb03319.x.
- [10] J. Jang, B.-G. Yoo, Y.-J. Kim, J.-H. Oh, I.-C. Choi, H. Bei, Indentation size effect in bulk metallic glass, Scr. Mater. 64 (2011) 753–756, https://doi.org/10.1016/j. scriptamat.2010.12.036.
- [11] H. Li, R.C. Bradt, The indentation load/size effect and the measurement of the hardness of vitreous silica, J. Non-Cryst. Solids 146 (1992) 197–212, https://doi. org/10.1016/S0022-3093(05)80492-2.
- [12] S.J. Bull, T.F. Page, E.H. Yoffe, An explanation of the indentation size effect in ceramics, Philos. Mag. Lett. 59 (1989) 281–288, https://doi.org/10.1080/ 09500838908206356
- [13] J. Gong, J. Wu, Z. Guan, Examination of the Indentation Size Eect in Low-load Vickers Hardness Testing of Ceramics, (n.d.).
- [14] J.B. Quinn, G.D. Quinn, Indentation brittleness of ceramics: a fresh approach, (n. d.).
- [15] A.A. Elmustafa, D.S. Stone, Indentation size effect in polycrystalline F.C.C. metals, Acta Mater 50 (2002) 3641–3650, https://doi.org/10.1016/S1359-6454(02) 00175-1
- [16] Z. Zong, J. Lou, O.O. Adewoye, A.A. Elmustafa, F. Hammad, W.O. Soboyejo, Indentation size effects in the nano- and micro-hardness of fcc single crystal metals, Mater. Sci. Eng. A 434 (2006) 178–187, https://doi.org/10.1016/j. msea.2006.06.137.
- [17] K. Durst, B. Backes, O. Franke, M. Göken, Indentation size effect in metallic materials: modeling strength from pop-in to macroscopic hardness using geometrically necessary dislocations, Acta Mater 54 (2006) 2547–2555, https://doi.org/10.1016/j.actamat.2006.01.036.
- [18] W.D. Nix, H. Gao, Size effects in crystalline: a law for strain gradient plasticity, (n. d.).
- [19] E.O. Bernhardt, Über die Mikrohärte der Feststoffe im Grenzbereich des Kick'schen Ähnlichkeitssatzes, Int. J. Mater. Res. 33 (1941) 135–144, https://doi.org/ 10.1515/ijmr-1941-330305.
- [20] Y. Shi, B. Deng, J. Neuefeind, Q. Zhou, M.M. Smedskjaer, S.R. Elliott, M. Bauchy, Revealing the effect of medium-range structure on silicate glass hardness, Phys. Rev. Mater. 7 (2023) 013602, https://doi.org/10.1103/ PhysRevMaterials.7.013602.
- [21] H. Li, A. Ghosh, Y.H. Han, R.C. Bradt, The frictional component of the indentation size effect in low load microhardness testing, J. Mater. Res. 8 (1993) 1028–1032, https://doi.org/10.1557/JMR.1993.1028.
- [22] M.V. Swain, M. Wittling, Fracture Mechanics of Ceramics, 11, Plenum, New York, 1996, p. 379, n.d.
- [23] S. Mannan, M. Zaki, S. Bishnoi, D.R. Cassar, J. Jiusti, J.C.F. Faria, J.F. S. Christensen, N.N. Gosvami, M.M. Smedskjaer, E.D. Zanotto, N.M.A. Krishnan, Glass hardness: predicting composition and load effects via symbolic reasoning-informed machine learning, Acta Mater 255 (2023) 119046, https://doi.org/10.1016/j.actamat.2023.119046.
- [24] K. Januchta, M.M. Smedskjaer, Indentation deformation in oxide glasses: quantification, structural changes, and relation to cracking, J. Non-Cryst. Solids X 1 (2019) 100007, https://doi.org/10.1016/j.nocx.2018.100007.
- [25] T. Rouxel, H. Ji, J.P. Guin, F. Augereau, B. Rufflé, Indentation deformation mechanism in glass: densification versus shear flow, J. Appl. Phys. 107 (2010) 094903, https://doi.org/10.1063/1.3407559.
- [26] M.M. Smedskjaer, M. Jensen, Y. Yue, Effect of thermal history and chemical composition on hardness of silicate glasses, J. Non-Cryst. Solids 356 (2010) 893–897, https://doi.org/10.1016/j.jnoncrysol.2009.12.030.
- [27] R.J. Hand, D.R. Tadjiev, Mechanical properties of silicate glasses as a function of composition, J. Non-Cryst. Solids 356 (2010) 2417–2423, https://doi.org/ 10.1016/j.jnoncrysol.2010.05.007.
- [28] M. Tiegel, R. Hosseinabadi, S. Kuhn, A. Herrmann, C. Rüssel, Young's modulus, Vickers hardness and indentation fracture toughness of alumino silicate glasses, Ceram. Int. 41 (2015) 7267–7275, https://doi.org/10.1016/j. ceramint.2015.01.144.
- [29] Y. Kato, H. Yamazaki, S. Itakura, S. Yoshida, J. Matsuoka, Load dependence of densification in glass during Vickers indentation test, J. Ceram. Soc. Jpn. 119 (2011) 110–115, https://doi.org/10.2109/jcersj2.119.110.
- [30] K. Nomura, Y.-C. Chen, R.K. Kalia, A. Nakano, P. Vashishta, Defect migration and recombination in nanoindentation of silica glass, Appl. Phys. Lett. 99 (2011) 111906, https://doi.org/10.1063/1.3637052.
- [31] M. Yamane, J.D. Mackenzie, Vicker's hardness of glass, J. Non-Cryst. Solids 15 (1974) 153–164, https://doi.org/10.1016/0022-3093(74)90044-1.
- [32] E.W. Taylor, Plastic deformation of optical glass, Nature 163 (323) (1949) 323, https://doi.org/10.1038/163323a0.
- [33] D.M. Marsh, A.H. Cottrell, Plastic flow in glass, Proc. R. Soc. Lond. Ser. Math. Phys. Sci. 279 (1997) 420–435, https://doi.org/10.1098/rspa.1964.0114.
- [34] R.W. Douglas, Some comments on indentation tests on glass, J Soc Glas Technol 42 (1958) 145–157.
- [35] F.M. Ernsberger, Role of densification in deformation of glasses under point loading, J. Am. Ceram. Soc. 51 (1968) 545–547, https://doi.org/10.1111/j.1151-2916.1968.tb13318.x.

- [36] J.R. Allwardt, J.F. Stebbins, B.C. Schmidt, D.J. Frost, A.C. Withers, M. M. Hirschmann, Letter. Aluminum coordination and the densification of highpressure aluminosilicate glasses, Am. Mineral. 90 (2005) 1218–1222, https://doi. org/10.2138/am.2005.1836.
- [37] M. Grimsditch, A. Polian, A.C. Wright, Irreversible structural changes in vitreous B2O3 under pressure, Phys. Rev. B 54 (1996) 152–155, https://doi.org/10.1103/ PhysRevB.54.152.
- [38] P.W. Bridgman, I. Šimon, Effects of very high pressures on glass, J. Appl. Phys. 24 (2004) 405–413, https://doi.org/10.1063/1.1721294.
- [39] M. Evers, Plastic deformation of glass with diamond indenters, Glas. Ber 40 (1967) 41–43.
- [40] K. Peter, Brittle fracture and microplasticity of glass in indentation experiments, Glas. Ber 37 (1964) 333–345.
- [41] S. Yoshida, J.-C. Sanglebœuf, T. Rouxel, Quantitative evaluation of indentationinduced densification in glass, J. Mater. Res. 20 (2005) 3404–3412, https://doi. org/10.1557/jmr.2005.0418.
- [42] T. Rouxel, H. Ji, T. Hammouda, A. Moréac, Poisson's ratio and the densification of glass under high pressure, Phys. Rev. Lett. 100 (2008) 225501, https://doi.org/ 10.1103/PhysRevLett.100.225501.
- [43] R. Chakraborty, A. Dey, A.K. Mukhopadhyay, Loading rate effect on Nanohardness of soda-lime-silica glass, Metall. Mater. Trans. A 41 (2010) 1301–1312, https://doi. org/10.1007/s11661-010-0176-8.
- [44] A. Dey, R. Chakraborty, A.K. Mukhopadhyay, Enhancement in nanohardness of soda-lime-silica glass, J. Non-Cryst. Solids 357 (2011) 2934–2940, https://doi. org/10.1016/j.jnoncrysol.2011.03.036.
- [45] R. Limbach, B.P. Rodrigues, L. Wondraczek, Strain-rate sensitivity of glasses, J. Non-Cryst. Solids 404 (2014) 124–134, https://doi.org/10.1016/j. inoncrysol.2014.08.023.
- [46] A. Bhattacharyya, G. Singh, K.Eswar Prasad, R. Narasimhan, U. Ramamurty, On the strain rate sensitivity of plastic flow in metallic glasses, Mater. Sci. Eng. A 625 (2015) 245–251, https://doi.org/10.1016/j.msea.2014.12.004.
- [47] V. Maier, K. Durst, J. Mueller, B. Backes, H.W. Höppel, M. Göken, Nanoindentation strain-rate jump tests for determining the local strain-rate sensitivity in nanocrystalline Ni and ultrafine-grained Al, J. Mater. Res. 26 (2011) 1421–1430, https://doi.org/10.1557/imr.2011.156.
- [48] B.N. Lucas, W.C. Oliver, G.M. Pharr, J.-L. Loubet, Time dependent deformation during indentation testing, MRS Proc 436 (1996) 233, https://doi.org/10.1557/ PROC 436-233
- [49] L. Shen, W.C.D. Cheong, Y.L. Foo, Z. Chen, Nanoindentation creep of tin and aluminium: a comparative study between constant load and constant strain rate methods, Mater. Sci. Eng. A 532 (2012) 505–510, https://doi.org/10.1016/j. msea.2011.11.016.
- [50] M.M. Chaudhri, Subsurface strain distribution around Vickers hardness indentations in annealed polycrystalline copper, Acta Mater 46 (1998) 3047–3056, https://doi.org/10.1016/S1359-6454(98)00010-X.
- [51] B.N. Lucas, W.C. Oliver, Indentation power-law creep of high-purity indium, Metall. Mater. Trans. A 30 (1999) 601–610, https://doi.org/10.1007/s11661-999-0051-7.

- [52] J.T. Hagan, Shear deformation under pyramidal indentations in soda-lime glass, J. Mater. Sci. 15 (1980) 1417–1424, https://doi.org/10.1007/BF00752121.
- [53] C. Hermansen, J. Matsuoka, S. Yoshida, H. Yamazaki, Y. Kato, Y.Z. Yue, Densification and plastic deformation under microindentation in silicate glasses and the relation to hardness and crack resistance, J. Non-Cryst. Solids 364 (2013) 40–43, https://doi.org/10.1016/j.jnoncrysol.2012.12.047.
- [54] W.C. Oliver, G.M. Pharr, An improved technique for determining hardness and elastic modulus using load and displacement sensing indentation experiments, J. Mater. Res. 7 (1992) 1564–1583, https://doi.org/10.1557/JMR.1992.1564.
- [55] H. Sawasato, S. Yoshida, T. Sugawara, Y. Miura, J. Matsuoka, Relaxation behaviors of Vickers indentations in soda-lime glass, J. Ceram. Soc. Jpn. 116 (2008) 864–868, https://doi.org/10.2109/icersi2.116.864.
- [56] S. Yoshida, S. Isono, J. Matsuoka, N. Soga, Shrinkage behavior of Knoop Indentations in Silica and Soda-Lime-Silica Glasses, J. Am. Ceram. Soc. 84 (2004) 2141–2143, https://doi.org/10.1111/j.1151-2916.2001.tb00976.x.
- [57] N.X. Randall, R. Christoph, S. Droz, C. Julia-Schmutz, Localised micro-hardness measurements with a combined scanning force microscope/nanoindentation system, Thin Solid Films 290–291 (1996) 348–354, https://doi.org/10.1016/ S0040-6000(65)09184-5
- [58] K. Hirao, M. Tomozawa, Microhardness of SiO2 glass in various environments, J. Am. Ceram. Soc. 70 (1987) 497–502, https://doi.org/10.1111/j.1151-2916.1987.tb05683.x.
- [59] W.C. Oliver, G.M. Pharr, Measurement of hardness and elastic modulus by instrumented indentation: advances in understanding and refinements to methodology, J Mater Res 19 (2004).
- [60] B.J. Koeppel, G. Subhash, Characteristics of residual plastic zone under static and dynamic Vickers indentations, Wear 224 (1999) 56–67, https://doi.org/10.1016/ S0043-1648(98)00328-7.
- [61] T.M. Gross, M. Tomozawa, Fictive temperature-independent density and minimum indentation size effect in calcium aluminosilicate glass, J. Appl. Phys. 104 (2008) 063529, https://doi.org/10.1063/1.2985907.
- [62] G. Constantinides, F.-J. Ulm, The nanogranular nature of C-S-H, J. Mech. Phys. Solids 55 (2007) 64–90, https://doi.org/10.1016/j.imps.2006.06.003.
- [63] C.G. Hoover, F.-J. Ulm, Experimental chemo-mechanics of early-age fracture properties of cement paste, Cem. Concr. Res. 75 (2015) 42–52, https://doi.org/ 10.1016/j.cemconres.2015.04.004.
- [64] M.J. Abdolhosseini Qomi, K.J. Krakowiak, M. Bauchy, K.L. Stewart, R. Shahsavari, D. Jagannathan, D.B. Brommer, A. Baronnet, M.J. Buehler, S. Yip, F.-J. Ulm, K. J. Van Vliet, R.J.-M. Pellenq, Combinatorial molecular optimization of cement hydrates, Nat. Commun. 5 (2014) 4960, https://doi.org/10.1038/ncomms5960.
- [65] J. Berthonneau, C.G. Hoover, O. Grauby, A. Baronnet, R.J.-M. Pellenq, F.-J. Ulm, Crystal-chemistry control of the mechanical properties of 2:1 clay minerals, Appl. Clay Sci. 143 (2017) 387–398, https://doi.org/10.1016/j.clay.2017.04.010.
- [66] J.H. Simmons, What is so exciting about non-linear viscous ow in glass, molecular dynamics simulations of brittle fracture and semiconductor±glass quantum composites. (1998).
- [67] J.H. Simmons, R. Ochoa, K.D. Simmons, J.J. Mills, Non-Newtonian viscous flow in soda-lime-silica glass at forming and annealing temperatures, J. Non-Cryst. Solids 105 (1988) 313–322, https://doi.org/10.1016/0022-3093(88)90325-0.